Journal of the Mechanics and Physics of Solids 134 (2020) 103774

Contents lists available at ScienceDirect

Journal of the Mechanics and Physics of Solids

journal homepage: www.elsevier.com/locate/jmps

Type IV failure in weldment of creep resistant ferritic alloys: I. Micromechanical origin of creep strain localization in the heat affected zone[☆]

Wei Zhang[a,b], Xue Wang[a], Yiyu Wang[b], Xinghua Yu[b], Yanfei Gao[a,*], Zhili Feng[b,*]

[a] Department of Materials Science and Engineering, University of Tennessee, Knoxville, TN 37996, USA
[b] Materials Science and Technology Division, Oak Ridge National Laboratory, Oak Ridge, TN 37831, USA

ARTICLE INFO

Article history:
Received 25 April 2019
Revised 28 October 2019
Accepted 30 October 2019
Available online 31 October 2019

Keywords:
Creep-strength-enhanced ferritic steel weldment
Microstructure-based finite element method
Grain boundary sliding
Strain localization

ABSTRACT

Creep strength enhanced ferritic (CSEF) steels containing 9-12wt% chromium have been extensively used in fossil-fuel-fired power plants. Despite their excellent creep resistance at high temperatures, premature failures (especially Type IV cracking) are often found in the fine-grained heat affected zone (HAZ) or intercritical HAZ of the welded components. This failure mode is preceded by the strain localization in the HAZ, as measured by the Digital Image Correlation (DIC) technique. The present work aims to develop a finite-element based computational method to determine the micromechanical and microstructural origin of the strain localization phenomenon. We construct a two-dimensional digital microstructure based on the actual microstructure of ferritic steel weldments by using the Voronoi-tessellation method, to account for the effects of its large grain-size gradients. A mechanism-based finite element method is developed for modeling the high temperature deformation resulting from a synergy of thermally activated dislocation movements, diffusional flow and grain boundary sliding. The numerical results agree well with the strain measurements by our DIC technique, particularly revealing the effect of pre-welding tempering on the evolution of strain localization in HAZ of creep resistant steel weldments. It is found that the diffusional creep with dependence on grain sizes, dislocation creep with dependence on material strength, and more importantly, grain boundary sliding, contribute synergistically to the creep strain accumulation in the HAZ, and their relative degree of significance is quantified. The creep rupture life will be investigated in the companion paper.

1. Introduction

Creep strength enhanced ferritic (CSEF) steels are widely used in ultra-supercritical (USC) fossil-fuel-fired power plants because of their excellent creep resistance and good thermal properties at high temperatures. During the long-term high

---

[☆] This manuscript has been authored by UT-Battelle, LLC under Contract No. DE-AC05-00OR22725 with the U.S. Department of Energy. The United States Government retains and the publisher, by accepting the article for publication, acknowledges that the United States Government retains a non-exclusive, paid-up, irrevocable, world-wide license to publish or reproduce the published form of this manuscript, or allow others to do so, for United States Government purposes. The Department of Energy will provide public access to these results of federally sponsored research in accordance with the DOE Public Access Plan (http://energy.gov/downloads/doe-public-access-plan).

[*] Corresponding authors.

E-mail addresses: ygao7@utk.edu (Y. Gao), fengz@ornl.gov (Z. Feng).

https://doi.org/10.1016/j.jmps.2019.103774
0022-5096/© 2019 Elsevier Ltd. All rights reserved.

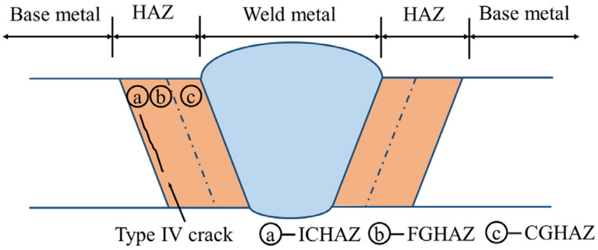

Fig. 1. Schematic illustration of Type- IV failure, which is located at the outer regime of HAZ.

temperature service, the creep performance of CSEF steel weldments is usually limited by the premature creep fracture in the fine-grained heat affected zone (FGHAZ) or intercritical heat affected zone (ICHAZ), as shown in Fig. 1, which is called the Type IV cracking. It is well acknowledged that the Type IV failure is preceded by the locally accumulated strain in the heat affected zone (HAZ) (Francis et al., 2006; Abson and Rothwell, 2013; Yu et al., 2014; Watanabe et al., 2006; Eggeler et al., 1994; Abe et al., 2008). Extensive studies have been performed to identify the causes for the deteriorated creep performance of the welded joints. It is suggested that the sharp microstructure and material property gradients in the HAZ result in significant creep strength degradation (Watanabe et al., 2006; Eggeler et al., 1994; Abe and Tabuchi, 2004; Tabuchi et al., 2001; Yu et al., 2013; Albert et al., 2004; Otoguro et al., 2000; Espositoa, 2016). Furthermore, the grain size, orientation of the fine grained HAZ, as well as the constraint from base metal and weld metal which leads to high triaxial stresses, all contribute to the deteriorated creep performance of the welded joints (Albert et al., 2004; Shinozaki and Kuroki, 2003). Although many creep tests and microstructural characterizations have been performed for weldments of CSEF steels, the underlying deformation mechanisms, which link the microstructure, material properties with creep performance, have not been fully understood, and a quantitative prediction of the degree of strain localization remains elusive.

CSEF steels typically form lath martensite microstructures after rapid quenching from austenite. The crystal plasticity constitutive models have been extensively used to simulate its plastic deformation, for example the cyclic plasticity under thermo-mechanical fatigue condition (Li et al., 2016), precipitate strengthen effects (Li et al., 2014) and its cyclic plastic deformation (Li et al., 2017), the high temperature deformation under multiaxial loading condition (Meade et al., 2018), and plastic deformation with presence of the hierarchical grain-pocket-block-lath microstructures (Sun et al., 2018, 2019). It is appropriate to utilize the crystal plasticity model to describe the anisotropic slip of crystalline materials when the plastic deformation is mainly caused by the dislocation glide. However, at high temperatures creep deformation of crystalline material usually results from a synergy of thermally activated diffusional flow, and grain boundary sliding (GBS), and dislocation movements (Frost and Ashby, 1982). Each of the three mechanisms may occur independently or compete against one another to be the dominant deformation mechanism under a certain loading condition. For a typical polycrystalline material, the plastic flow at high temperatures is mediated by Coble creep through grain boundary diffusion (Coble, 1963) or Nabarro–Herring creep through lattice diffusion (Nabarro, 1967; Herring, 1950) under low applied stresses, by dislocation creep through lattice or dislocation core diffusion at high stresses, and by grain boundary sliding at intermediate stress regime especially in fine grained materials. In order to simulate the high temperature deformation of crystalline material under a wide range temperature and stress levels, a comprehensive computational model is required, which is capable to incorporate the above physical mechanisms. Bower and Wininger (2004) developed a mechanisms-based finite element framework to model the grain boundary sliding, grain boundary diffusion and migration, as well as thermally activated dislocation creep of polycrystalline materials. Their simulation results reflect a deformation-mechanism transition from dislocation creep controlled plasticity in materials with coarse grain sizes at high strain rates to grain boundary sliding and diffusion dominated plasticity in fine grained materials at low strain rates. The mechanisms-based finite element methods were also used to investigate the deformation of nanocrystalline materials (Wei et al., 2007; Wei et al., 2008; Li et al., 2009), in which grain boundary deformation, e.g., grain boundary sliding and diffusion, was found to play significant roles in the determination of the macroscopic response of small-grained materials. The continuum level finite element simulations show the unique advantage in analyzing the microstructure evolution, grain-scale deformation, and the global-local deformation relationships of polycrystalline materials. A typical CSEF steel weldment shows microstructure gradients and heterogeneous material properties in different material zones. Most of the current computational models account for the heterogeneous material properties by compiling the welds with multiple zones, in which each zone is represented by different constitutive parameters while the constitutive law is the same for all these zones (Watanabe et al., 2006; Shinozaki and Kuroki, 2003; Gaffard et al., 2005; Petry and Gariboldi, 2010; Yaguchi et al., 2010; Masse and Lejeail, 2013; Basirat et al., 2015; Hall and Hayhurst, 1991; Hayhurst et al., 2005). Radically different from those in literatures, the present work proposes a microstructure-based computational model that can explicitly consider the key microstructure features and assist the simulation for the creep deformation of CSEF steel weldments on the grain length scale.

The present work aims to develop a high temperature mechanisms-microstrcture-based computational model which is capable of predicting weld creep deformation over a wide range of stress and temperature of interest. The remaining of the paper is organized as follows. In Section 2, creep tests were performed on the modified 9Cr-1Mo steel cross-weld samples,

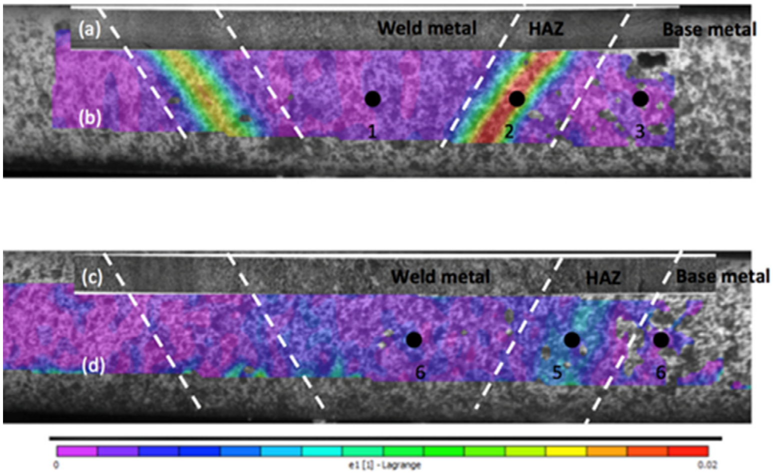

Fig. 2. Full field strain maps obtained using DIC and metallographs for standard pre-weld tempering condition (b, a) and non-standard pre-weld tempering condition (d, c) Grade 91 steel weldments after 85 h creep at 650 °C and 70 MPa (Yu et al., 2014).

and Digital Image Correlation (DIC) technique was utilized to measure the full field deformation map. In Section 3, a two-dimensional microstructure-informed model with large grain size gradients is constructed to represent the heterogeneous microstructure of welded joints. In Section 4, we list the assumptions and constitutive laws for the high temperature deformation mechanisms which are responsible for creep deformation of CSEF steel welds, including the thermally activated dislocation creep, diffusional flow as well as grain boundary sliding. In Section 5, the material parameters for the computational model are calibrated with the experimental creep data. Application and validation of our proposed model to represent the deformation response of ferritic steel weldments is reported in Section 6. The concluding remarks are given in Section 7.

2. Experiments

2.1. Material and experimental procedure

The material examined here is ASTM Grade 91, and the chemical composition is Fe-0.08C-8.61Cr-0.89Mo-0.27Mn-0.11Si-0.09Ni-0.21V-0.07Nb-0.06N, in weight percent. Current investigation studies the weld creep performance of two pre-welding temper conditions, with one plate (25.4 mm thick) tempered at 760 °C (designated as *standard condition* (ASTM 2008)) and the other plate tempered at 650 °C (designated as *non-standard condition*). Both plates were tempered for one hour before the welding was performed. The plates were machined on the edge with an angle of 37.5° to make a double-V groove. The grooved plates were pre-heated in a furnace that was set 120°C. The welded joints of Grade 91 were prepared by means of Gas Tungsten Arc welding (GTAW) using the filler metal (Fe-0.08C-8.62Cr-0.92Mo-0.41Mn-0.31Si-0.15Ni-0.24V-0.08Nb-0.04N) of similar chemical composition as the base metal. Welding current, voltage and speed were 260 A, 8 V and 2.5 mm/s respectively. The welded plates were post-weld heat treated (PWHT) at 760 °C for 2 h, followed by air-cooling to room temperature.

Tensile creep-rupture tests of the weld cross-sections were performed at 650 °C and 70 MPa, using a Gleeble$^{\mathrm{TM}}$ thermal mechanical simulator. Samples were machined to 7 mm diameter rod with a gage length of 70 mm. The creep-rupture tests were interrupted at 85 h. During testing, the DIC technique was used to measure the local creep strain in the cross-weld samples. DIC uses a 3D camera system to capture the optical images of the sample surface that is coated with a high contrast random dot patterns, and the relative positions of the patterns on the sample surface are correlated to one another to calculate the local strain as a function of time. Digital cameras (Point Grey GRAS-50S5C-C) linked with a computer were used for image acquisition. Sigma lenses (28–300 mm f/3.5-6.3 DG) were used for zooming purpose. Since the thermal radiation from the hot sample at elevated temperature will lessen image contrast, the present study adopted monochromatic light illumination and narrow bandpass filter to reduce the DIC measurement errors. The 3×4 high-brightness green LED array (Visual Instrumentation model 900405, wavelength 530±5 nm) and Edmund 532 nm hard-coated bandpass filter (Part number 65155) were used. Images were taken at 1 min intervals for the first 12 h and then at 5 min intervals for the subsequent 78 h. Images were post-processed by the Vic-3D software developed by Correlated Solutions (Solutions, 2010). DIC measurement covered the region of interest in the middle of each sample, which is about 4 mm by 20 mm in area, as shown in Fig. 2.

The microhardness traverse of the cross-weld specimens was determined utilizing a Leco LM-100AT hardness tester. Dwell time for hardness testing was 12 seconds. Microstructural details can be found in our previous report (Yu et al., 2014).

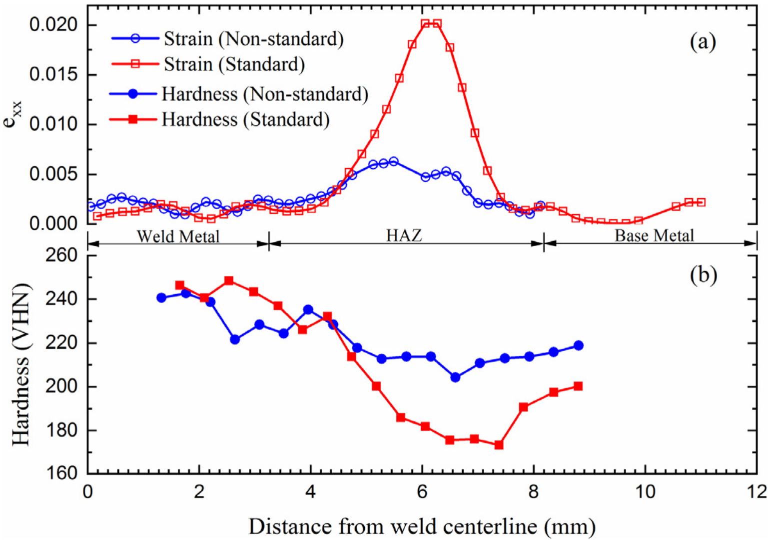

Fig. 3. (a) Distribution of transverse creep strain, and (b) hardness profile for the Grade 91 steel weldments (Yu et al., 2014).

2.2. Experimental results

The full field strain maps after 85 h of creep in the center of the samples are shown in Fig. 2(b) and (d) for the standard condition and nonstandard condition samples, respectively. In order to identify different regions, the optical macrographs on the polished and etched surface were obtained and overlapped with strain maps, as shown in Fig. 2(a) and (c). The strain maps exhibit inhomogeneous creep deformation. Particularly, two distinct regions with high strain were observed in the standard condition sample, where most of deformation is concentrated in the HAZ. Nevertheless, no significant strain localization is observed in the non-standard condition sample. After 85 h stress-rupture test, creep strain in HAZ of standard condition is as high as 2.05 %. Even though strain map of non-standard condition does not show prominent localized deformation in HAZ due to the color scale used, final strain (0.60 %) in HAZ is much higher than that in weld metal and base metal. Both conditions show near zero creep deformation in base metals. Similar phenomenon was also seen in weld metal that there is no difference between standard and non-standard samples. The result implies both weld metal and base metal microstructure and creep properties are of the least importance in a welded structure. In other words, creep deformation predominantly accumulates in the HAZ.

The traverse strain ε_{xx} plot from weld metal to base metal after 85 h of creep is shown in Fig. 3(a), and the corresponding hardness plot is shown in Fig. 3(b). Clearly, the peaks in traverse strain curve represent the significant creep deformation in the HAZ. Both peaks have a width of 4 mm, which is larger than the measured width of the FGHAZ (about 2 mm). As a result, this localized creep deformed region may include both FGHAZ and ICHAZ. Weld metal hardness for both conditions is the same and has the highest value (about 240 VHN) compared with HAZ and base metal. For non-standard condition, hardness from 4.4 mm to 8 mm (about 210 VHN) is 30 VHN lower than that in weld metal. The low hardness region is the same region that has high creep deformation. Base metal hardness of non-standard condition is about 210 VHN, which is slightly higher than the hardness of HAZ. One the other hand, a large dip is observed in the hardness distribution of the standard condition. The lowest hardness is 170 VHN, which is 70 VHN lower than hardness in weld metal and 30 VHN lower than that in base metal. The low hardness region is also from 4.4 mm to 8 mm, which is the same as non-standard condition.

The difference in creep properties can be correlated with the precipitate distribution in the FGHAZ of the standard and non-standard pre-weld tempering weldments of Grade 91 steel (Yu et al., 2014), as shown in Fig. 4. In the standard pre-weld tempering condition, the precipitate $M_{23}C_6$ (M=Cr, Fe) in the FGHAZ is of the near-equilibrium condition, and it is mainly distributed on the prior austenite grain boundaries (PAGBs), martensite block and pocket boundaries. While in the nonstandard condition, as the tempering is not complete, the $M_{23}C_6$ in the FGHAZ is much smaller, and it is almost completely dissolved into the matrix during the welding thermal cycles. $M_{23}C_6$ would reprecipitate on the fine prior austenite grain boundaries and martensite block boundaries when the sample is subjected to PWHT. The MX (M=Nb, V; X=C, N) phase remains stable and shows the similar distribution in both conditions. The difference in the distribution of $M_{23}C_6$ phase is believed to induce the improved creep properties of the nonstandard pre-weld tempering weldment, as the finer $M_{23}C_6$ on the grain boundaries can effectively pin the grain boundary movement and stabilize the martensite substructures. The investigation of the precipitate effects will be left for a future study.

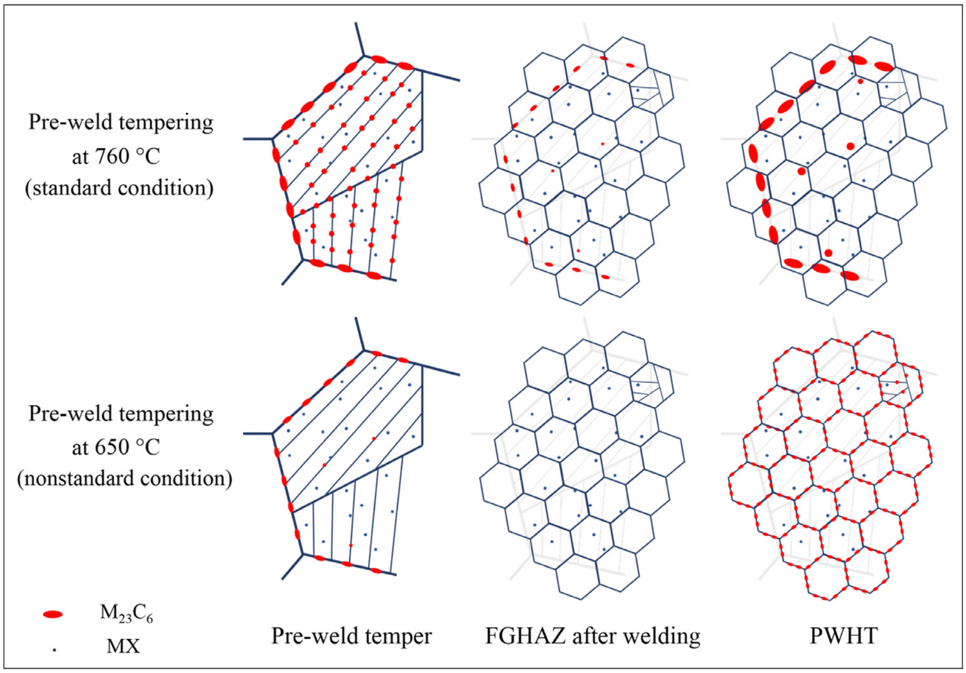

Fig. 4. Schematic microstructure evolution of the FGHAZ during pre-weld tempering, welding, and PWHT for the standard and nonstandard pre-weld tempered weldments of Grade 91 steel.

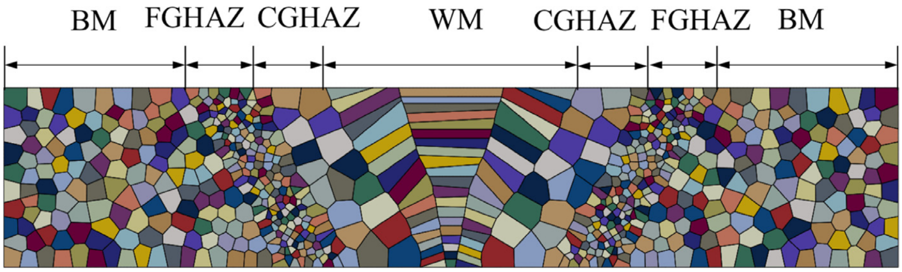

Fig. 5. Two-dimensional digital microstructure model for ferritic steel weldment with grain size gradients in the base metal (BM), fine grained heat-affected zone (FGHAZ), coarse grained heat-affected zone (CGHAZ), and weld metal (WM).

3. Microstructural model

As the materials joined together by fusion arc welding processes, the rapid heating/cooling thermal cycles introduces significant changes in the microstructure between the base metal and weld metal, and a transition region, i.e., HAZ, is formed consequently. In order to consider the microstructural heterogeneities of the welded joints, we construct a two-dimensional digital microstructure by using Voronoi tessellation method in an open source software Neper (Quey et al., 2011). As shown in Fig. 5, the simplified digital microstructure agrees well with a typical weldment in its topological and structural properties. There are strong grain size gradients in WM, CGHAZ, FGHAZ, ICHAZ, and BM. In the present study, the focused region is the fine-grained HAZ where creep strain accumulates significantly and Type IV failure takes place during the long-term loading conditions (Yu et al., 2014; Watanabe et al., 2006; Abe and Tabuchi, 2004; Tabuchi et al., 2001; Gaffard et al., 2005; Tabuchi et al., 2009). For ease of implementation, ICHAZ and FGHAZ are not differentiated, as they both essentially have fine-grained microstructures after post-weld heat treatment. The two-dimensional microstructure contains 750 grains, and each one is assumed to have random crystallographic orientation. Note the colors in Fig. 5 only represent the boundaries of each grain and have no specific meaning like grain orientations. The average grain sizes of FGHAZ and the other regions (BM, CGHAZ and WM) are assumed to be 1 μm and 5 μm, respectively. Taking advantage of the digital microstructure, we considered the influences of microstructural heterogeneities (e.g., orientation and shape of all grains, and gradient in the grain size), as well as heterogeneous material properties on the scale of individual grains (e.g., hardness variation, heterogeneous grain boundary diffusivity, and grain boundary sliding resistance that is related to grain boundary precipitates). The present work is among the first to model the creep deformation of weldments with explicit representation of microstructure gradients, which, as will be shown later, play a significant role in the overall and local deformation of weldments.

4. Constitutive models

In the following, we will present a mechanisms-based constitutive model for the analysis and prediction of the high temperature creep deformation of CSEF steel weldments. The computational framework accounts for the combined effects of grain interior dislocation creep and diffusional creep as well as grain boundary sliding, that is, to couple a creep constitutive model for the grain interior deformation with a viscous interface model for grain boundary sliding. It is worth noting again that GBS is not included in the Ashby maps, because such a deformation mechanism has to be integrated with other accommodating mechanisms and cannot stand alone. An explicit microstructural simulation is needed especially when grain size gradient exists like in our applications.

4.1. Constitutive equations for the grain interior

It is commonly accepted that the main plastic deformation of grain interior results from diffusional creep and dislocation creep at high temperatures. The steady-state creep rates of different mechanisms are generally described by the well-known Mukherjee-Bird-Dorn equation (Mukherjee et al., 1969):

$$\dot{\varepsilon}_{ss} = \frac{ADEb}{k_B T}\left(\frac{b}{d}\right)^p \left(\frac{\sigma}{E}\right)^n, \tag{1}$$

where $\dot{\varepsilon}_{ss}$ is the steady state creep rate; σ is the applied stress; k_B and T are the Boltzmann's constant and the absolute temperature, respectively; E is the Young's modulus; b is the Burgers vector, d is the grain size; p is the inverse grain size exponent; n is the stress exponent; A is a material dependent constant; and D is the diffusion coefficient represented by Arrhenius law,

$$D = D_0\, exp(-Q/RT), \tag{2}$$

where Q is the activation energy for the diffusion process, and D_0 is the diffusion pre-exponent. Each creep mechanism can be characterized by Eq. (1) with specific values of diffusivity D, activation energy Q, inverse grain size dependence p and stress exponent n. For diffusional creep, they are the lattice diffusion controlled Nabarro-Herring creep and the grain boundary diffusion governed Coble creep. As the Nabarro-Herring creep only occurs at extremely high temperature ($\sim 0.8T_M$) due to its high activation energy (Frost and Ashby, 1982), in the present analysis solely Coble creep is considered as the operating diffusional flow, which is characterized by stress exponent $n = 1$ and inverse grain size exponent $p = 3$. In the majority of alloys, at high temperatures the dislocation climb is required when the gliding dislocation is held by physical obstacles, in which transport of matter is through lattice diffusion. Therefore, the lattice diffusion-controlled dislocation creep ($n \geq 4$) is considered as another contribution to the grain interior deformation, which shows no dependence on grain size.

Based on the above discussions, a creep constitutive model for grain interior deformation has been developed, with presence of both dislocation creep and Coble creep. The strain rates are decomposed into elastic and plastic parts,

$$\dot{\varepsilon}_{ij} = \dot{\varepsilon}^{e}_{ij} + \dot{\varepsilon}^{p}_{ij}. \tag{3}$$

The elastic deformation follows the generalized Hooke's law,

$$\dot{\varepsilon}^{e}_{ij} = \frac{1+\nu}{E}\left(\dot{\sigma}_{ij} - \frac{\nu}{1+\nu}\dot{\sigma}_{kk}\delta_{ij}\right). \tag{4}$$

As the creep deformation mechanisms are independent of each other, the strain produced by each mechanism contributes additively to the total creep deformation. The creep rate equation is generalized to multiaxial stress state as followings:

$$\dot{\varepsilon}^{p}_{ij} = \left[A_{dis}\frac{EbD_l}{k_B T}\left(\frac{\sigma_e}{\sigma_0}\right)^n + A_{coble}\frac{EbD_{gb}}{k_B T}\left(\frac{b}{d}\right)^3\left(\frac{\sigma_e}{E}\right)\right]\frac{3S_{ij}}{2\sigma_e}, \tag{5}$$

where the two terms represent the contribution of dislocation creep and Coble creep, respectively, S_{ij} is the deviatoric stress tensor $\sigma_{ij} - \sigma_{kk}\delta_{ij}/3$, and σ_e is the von Mises stress $\sqrt{3S_{ij}S_{ij}/2}$. The diffusivity coefficients for the dislocation creep D_l and Coble creep D_{gb} obey the Arrhenius law,

$$D_l = D_{0l}\, exp(-Q_l/RT), \tag{6a}$$

$$D_{gb} = D_{0gb}\, exp\left(-Q_{gb}/RT\right), \tag{6b}$$

where the pre-exponents for lattice diffusion D_{0l} and grain boundary diffusion D_{gb}, and the activation energies for lattice diffusion Q_l and grain boundary diffusion Q_{gb} all can be found in the literature (Abe et al., 2008; Frost and Ashby, 1982).

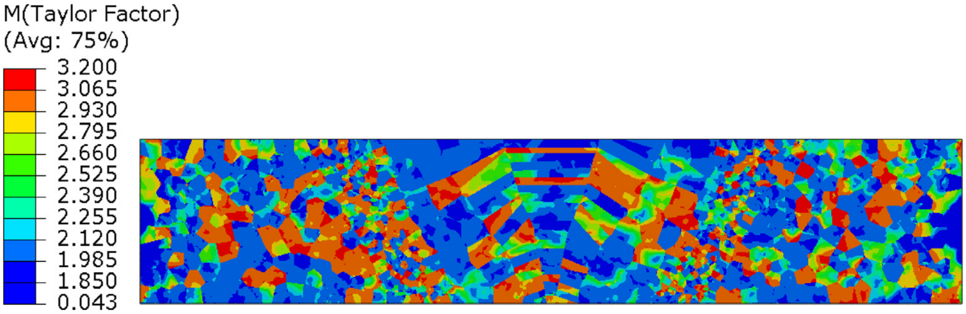

Fig. 6. Contour plot of the micromechanical Taylor factor for ferritic steel weldment to represent the crystallographic orientation of each individual grain (each grain assigned with random orientations).

The only unknowns, the dimensionless material constants A_{dis},A_{coble} and the stress exponent n for dislocation creep, will be determined via calibration with experimental creep data in Section 3.

In order to represent the anisotropic nature of crystal slips induced by crystallographic orientation effect of each individual grain, we introduce a micromechanical Taylor factor (Raabe et al., 2001). It is defined as the ratio between the local crystallographic shear $\sum \gamma^{\mathrm{local}}$ and the local von Mises strain $\langle \varepsilon_{\mathrm{VM}}^{\mathrm{local}} \rangle$ within each grain,

$$M = \frac{\sum \gamma^{\mathrm{local}}}{\langle \varepsilon_{\mathrm{VM}}^{\mathrm{local}} \rangle}, \tag{7}$$

where $\sum \gamma^{\mathrm{local}}$ and $\langle \varepsilon_{\mathrm{VM}}^{\mathrm{local}} \rangle$ are numerically calculated by using a separate crystal plasticity simulation (Huang, 1991). The results for the micromechanical Taylor factors are shown in Fig. 6. High values of the Taylor factor indicate the grain with certain crystallographic orientation is geometrically soft, where the crystal slips are preferable to occur. In the weldment, dislocation creep strain percolation follows grains which are geometrically soft and avoids grains those are hard. The grain orientation effect has been incorporated into the dislocation creep as,

$$\dot{\varepsilon}_{ij}^{\mathrm{p}} = \left[A_{\mathrm{dis}} \bar{M}^{\mathrm{I}} \frac{EbD_{\mathrm{l}}}{k_{\mathrm{B}}T} \left(\frac{\sigma_{\mathrm{e}}}{\sigma_0} \right)^n + A_{\mathrm{coble}} \frac{EbD_{\mathrm{gb}}}{k_{\mathrm{B}}T} \left(\frac{b}{d} \right)^3 \left(\frac{\sigma_{\mathrm{e}}}{E} \right) \right] \frac{3S_{\mathrm{ij}}}{2\sigma_{\mathrm{e}}}, \tag{8}$$

where $\bar{M}^{\mathrm{I}}$ is the normalized micromechanical Taylor factor for the I_{th} grain, $\bar{M}^{\mathrm{I}} = M^{\mathrm{I}} / \max(M^1, M^2, \ldots, M^{\mathrm{I}}, \ldots, M^{\mathrm{N}})$, and N is the total number of grains within the polycrystalline model. The numerical procedure of the grain interior creep constitutive model is implemented in the commercial finite-element software ABAQUS (ABAQUS, 2012) via a user-defined material model (UMAT).

The above modeling framework, by incorporating the micromechanical Taylor factor, can be justified via the following considerations. First, as will be shown later, our experiments were conducted at 70 MPa on Grade 91 ferritic steel, which falls into the transition between dislocation creep and Coble creep regimes in Fig. 8 (NIMS data, 1996). In the companion paper, the lifetime data (again from NIMS) are investigated in a regime where the applied stress is lower than 70 MPa and the lifetime is longer than thousands of hours. Under these conditions, the deformation is very much governed by GBS and Coble creep, and the failure is by diffusional void growth on the grain boundaries. To this end, more advanced crystal plasticity models, especially these developed in (Wei et al., 2008; Li et al., 2009; Gaffard et al., 2005; Petry and Gariboldi, 2010; Yaguchi et al., 2010; Masse and Lejeail, 2013), are not employed, since the micromechanical Taylor factor already takes in consideration the grain orientation effect. Second, results in Fig. 6 are based on {110}<111> slip systems without hardening by using the UMAT in Nieh et al. (1998). Two hardening laws (Bassani-Wu and Peirce-Asaro-Needleman) have been employed for comparison purpose, which are implemented in Nieh et al. (1998) based on the slip strain rates. We also conducted simulations based on a more advanced model in Shrestha et al. (2012; Kimura et al. (2007), which adopts the dislocation densities as state variables that are loosely connected to the pocket-block-lath microstructure. All these additional simulations show little difference from the results in Fig. 6. Third, our model in Eq. (8) is especially advantageous in large scale simulations because the crystal plasticity models usually have difficulty in converging. This becomes more apparent in the companion paper when voids are incorporated in the grain boundaries.

4.2. Constitutive model for grain boundary

Grain boundary sliding is one of the competing mechanisms that contribute to the creep deformation and damage of ferritic steel weldments (Abson and Rothwell, 2013; Abe et al., 2008; Basirat et al., 2015; Kimmins and Smith, 1998; Basirat et al., 2012). In general, GBS, controlling the strain rate sensitivity in the intermediate stress regime, is the main deformation mechanism for superplasticity of polycrystalline materials (45). In the literature GBS is usually considered as a rate contribution to the grain interior deformation and characterized by the grain size dependence $p = 2, 3$ and stress exponent

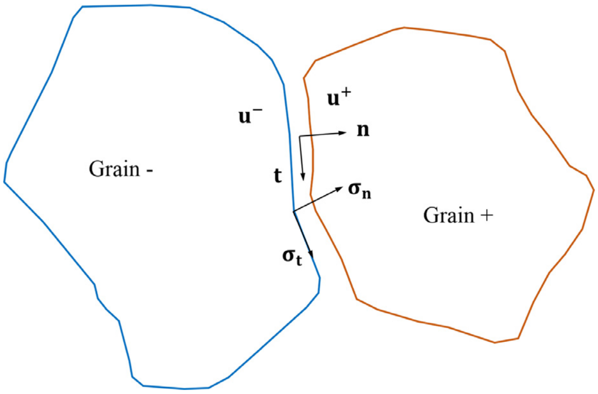

Fig. 7. A representative grain boundary with displacement $\boldsymbol{u}^+$ and $\boldsymbol{u}^-$ across the boundary, normal $\boldsymbol{n}$ and tangential $\boldsymbol{t}$ directions, as well as normal σ_n and tangential σ_t tractions.

$n = 2$ (Nieh et al., 1998). Even though this treatment of GBS provides quantitative creep rate, it has no obvious effect on the stress distribution and cavity formation of polycrystalline materials. In fact, GBS on the other hand significantly influences the stress multiaxiality which has direct effects on the creep cavitation and crack development (Shinozaki and Kuroki, 2003; Yaguchi et al., 2010). Furthermore, the large microstructural gradients of ferritic steel weldments require explicit modeling of grain boundary sliding.

GBS is assumed as a thermally activated process, driven by shear tractions acting tangentially to the grain boundary, and it obeys the Newtonian viscous law,

$$\dot{u}_\mathrm{t} = \frac{\Omega \eta_0 \exp\left(-Q_\mathrm{gbs}/RT\right)}{k_\mathrm{B} T} \sigma_\mathrm{t}, \tag{9}$$

where $u_\mathrm{t} = (\boldsymbol{u}^+ - \boldsymbol{u}^-) \cdot \boldsymbol{t}$ denotes the relative tangential displacement across the grain boundary in response to the local shear traction σ_t, as shown in Fig. 7, η_0 is a characteristic sliding velocity, Ω is the atomic volume and Q_gbs is the activation energy. The numerical procedure of grain boundary sliding is implemented in ABAQUS (ABAQUS, 2012) by developing a cohesive interface model via the user-defined element (UEL). From geometric point of view, GBS cannot occur in a polycrystalline solid in absence of some other deformation mechanisms. It usually requires accommodation from diffusional flow, grain boundary migration or dislocation creep, to diminish the incompatible velocity discontinuity across the grain boundaries (Bower and Wininger, 2004; Nieh et al., 2005; Gifkins, 1976). In the present work, the coupling between GBS, dislocation creep, and diffusional flow accommodates the discontinuous velocity field naturally as a consequence of enforcing compatibility and equilibrium on the overall deformation using the finite element method.

5. Calibration of material parameters

Applying the proposed constitutive models for analysis of the creep deformation of CSEF steel weldments, we need to estimate the values for the material constitutive parameters. Most of the them can be found in the literatures (Eggeler et al., 1994; Abe et al., 2008; Frost and Ashby, 1982; Shrestha et al., 2012), and the only unknown material parameters (e.g., dimensionless coefficient A_dis and A_Coble, and stress exponent n) will be determined through calibration with experimental creep rate data. The creep deformation of CSEF steels and their weldments has been experimentally studied by numerous researches (e.g., (Yu et al., 2014; Watanabe et al., 2006; Eggeler et al., 1994; Gaffard et al., 2005; Tabuchi et al., 2009; Shrestha et al., 2012; Kimura et al., 2007; Choudhary and Samuel, 2011; 51)). Most laboratory experiments performed short-term creep tests at high applied stresses, however, the knowledge for long-term creep at low stress level is required for development of a comprehensive model. In the present study, the NIMS (51) and Shrestha et al. (2012) creep data of Grade 91 steels, as shown in Fig. 8, are selected as they cover a wide range of applied stress levels. It is observed the creep rate of Shrestha et al. (2012) is about one order of magnitude higher than that of the NIMS data (51) especially in the low stress regime. This kind of creep rate scatter for Grade 91 steels is commonly reported in the literature (Abe, 2016), which can be resulted from differences in chemical compositions and heat treatment conditions, etc. In the present work, the NIMS creep strain rate vs. stress curve is used as a reference dataset to calibrate the unknown material parameters for the computational model. As shown in Fig. 8, the calibration of Coble creep coefficient is performed for stresses below 60 MPa, where the diffusional creep is expected to be dominant. By fitting the low stress zone with Coble creep (stress exponent $n = 1$), the dimensionless coefficient $\mathrm{A}_\mathrm{Coble}$ is determined as $6.237 \times 10^{-3} \mathrm{s}^{-1}$. The material parameters for dislocation creep are obtained by fitting the power-law creep rate with the experimental data in high stress regime. The stress exponent for the dislocation creep, i.e. the slope of the $log(\dot{\varepsilon}) - log(\sigma)$ curve, is identified as $n \approx 8$, and the corresponding coefficient for dislocation creep A_dis is determined as $16.0 \mathrm{s}^{-1}$. The representative values for the material parameters used as model inputs are listed in the Table 1.

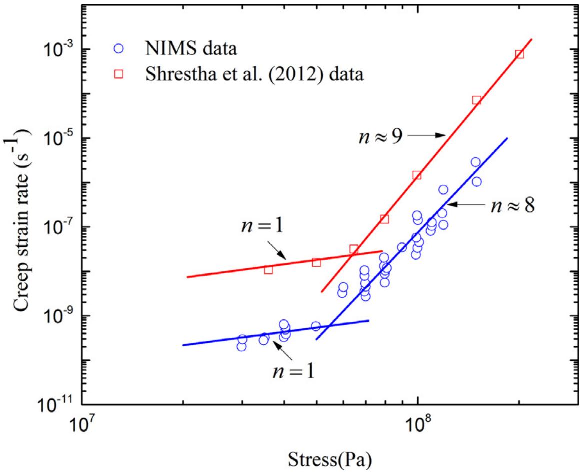

Fig. 8. Stress dependence of steady state creep rate for Grade 91 ferritic steel at 650 °C.

Table 1
Representative values for material parameters used in the computational model. Parameters related to the thermal activation processed are fitted from the NIMS data.

Parameter	Value
Atomic volume, Ω	1.18×10^{-29} m^3
Melting temperature, T_M	1810K
Burgers vector, b	2.48×10^{-10} m^3
Young's modulus, E_0	223 GPa
Young's modulus at 923K, E	90.14 GPa
Poisson's ratio, ν	0.3
Grain boundary diffusion pre-exponent, D_{0gb}	0.0044m^2/s
Grain boundary diffusion activation energy, Q_{gb}	174KJ/mole
Coble creep coefficient, A_{coble}	6.237×10^{-3} s^{-1}
Lattice diffusion pre-exponent, D_{0l}	0.021m^2/s
Lattice diffusion activation energy, Q_l	500KJ/mole
Dislocation creep coefficient, A_{dis}	16.0 s^{-1}
Reference stress, σ_0	90.14 MPa
Stress exponent, n	8
Grain boundary sliding pre-exponent, η_0	40m/s
Average grain size in FGHAZ, d	1 µm
Average grain size in the other zones, d	5 µm

6. Application of the model to ferritic steel weldment

The proposed computational model is applied to investigate the micromechanical and microstructural origin for the creep deformation and strain localization phenomenon in the CSEF cross-welds. The effects of pre-weld tempering will also be discussed. The numerical simulations are validated and compared with the strain field measurement in Yu et al. (2014) and Fig. 2. In Section 6.1, the grain size effect is investigated with respect to Coble creep and dislocation creep, while the hardness variation of the non-standard and standard pre-welding tempering weldments is considered in Section 6.2. In Section 6.3, GB sliding in incorporated based on Section 6.2. The contribution of Coble creep, dislocation creep, and grain boundary sliding to the total plastic deformation for Grade 91 steel welds will be quantified step-by-step. The following simulations are of same boundary and loading conditions as the experimental creep tests, i.e., the microstructure model as shown in Fig. 5 is fixed on the left side, loaded and hold at 650°C/70 MPa for 85 h on the right side along the transverse direction.

6.1. Coble creep and grain size effect

Coble creep, governed by grain boundary diffusion, is a dominant contributor to the plastic deformation for materials at high temperatures and low stresses, especially for small grained materials. In this section, the contribution of Coble creep (part of grain size effect) for Grade 91 steel welds will be quantified. As presented in Section 4.1, the dislocation creep is independent of grain size, whereas the strain rate of Coble creep is proportional to d^{-3} (d is the grain size). To differentiate the Coble creep from the others, different material regions are assumed with the same creep strength but different grain sizes. Noted the non-standard and standard pre-welding tempered weldments are assumed to have same grain size distri-

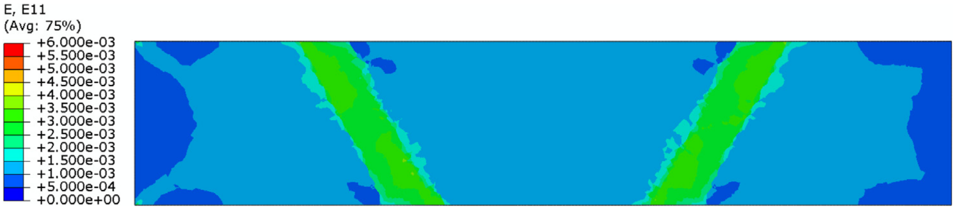

Fig. 9. Contour plot of the strain distribution for Grade 91 steel weldment after 85 h creep at 650 °C and 70 MPa, only considering the grain size effects.

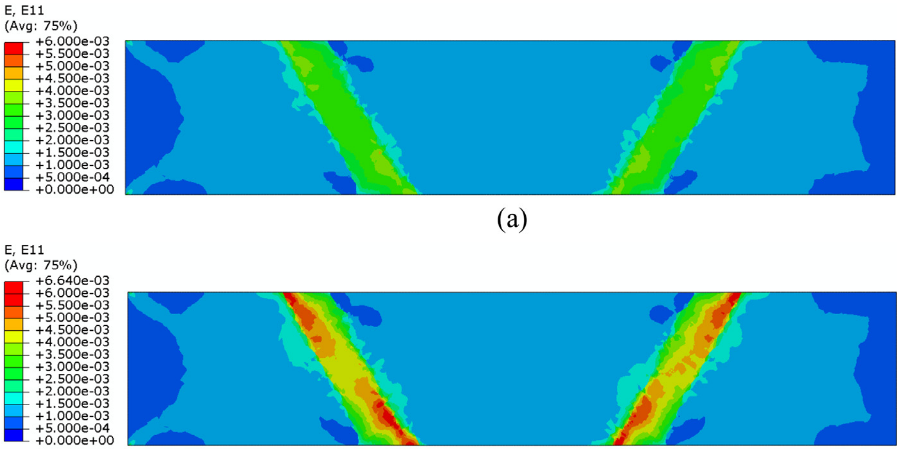

(a)

(b)

Fig. 10. Contour plot of the full field strain in presence of the variation of both grain size and hardness, (a) for non-standard condition weldment with 7 % hardness reduction in HAZ, and (b) for standard condition weldment with 23 % hardness reduction in HAZ, after 85 h creep at 650 °C and 70 MPa.

bution (Fig. 5), as both treatment welds show similar fine martensitic microstructures in the FGHAZ (Yu et al., 2013). Fig. 9 shows the numerical results for the strain field of the Grade 91steel weldment under 70 MPa loading and holding for 85 h at 650 °C. The strain map shows most of the deformation is concentrated in the FGHAZ. The creep strain of fine-grained HAZ (~ 0.3 %) is about two times higher than that of the base metal and weld metal (~ 0.1 %), which is resulted from the accelerated Coble creep in the fine-grained HAZ. While decreasing the applied stress level, Coble creep will gradually take the leading role for the creep deformation because of the low activation energy for GB diffusion. The present numerical simulation clearly shows grain size dependent Coble creep plays an important role in the high temperature creep deformation and strain concentration in the FGHAZ of Grade 91 steel welds.

6.2. Dislocation creep and hardness variation effect

The hardness profiles of the non-standard and standard treatment Grade 91 steel weldments both exhibit minimum value in the vicinity of fine-grained HAZ, as shown in Fig. 3(a). This region is commonly regarded as the weakest link in welded joints, which shows susceptibility to Type IV crack after long-term creep service. The following numerical simulations, accounting for the grain interior deformation, are employed to study the effect of hardness on creep behavior of Grade 91 steel weldments. The dislocation creep is strongly dependent on the material strength. its creep strain rate is a function of the reference stress σ_0, which is a representation of material strength and assumed to be proportional to the hardness. Fig. 10 shows the numerical results for the strain field of both nonstandard and standard treatment weldments after 85 h of creep at 70 MPa and 650 °C. The numerical simulations incorporate the variation of both hardness and grain size for the weldments. Compared to the strain field obtained in Section 6.1 (Fig. 9), there is additional strain concentration in the fine-grained HAZ (e.g., standard condition 0.58%). That is, in addition to Coble creep, dislocation creep with dependence on material strength also contributes to the strain localization in Grade 91 steel weldments.

The strain localization in the fine-grained HAZ of standard condition is much more significant than that of the non-standard condition. Based on the hardness measurement, it can be deduced that the dislocation creep rate of the fine-grained HAZ is increased by 1.787 and 8.092, respectively, compared to that of the base metal of the non-standard and standard treatment weldments. However, the dislocation creep is not as high as the theoretical analysis because the ‘soft’ HAZ is mechanically constrained by the ‘hard’ base metal and weld metal. Triaxial stress state forms due to the constraint effect, and accordingly it lowers the effective stress and dislocation creep rate of the FGHAZ. Dislocation creep will gradually

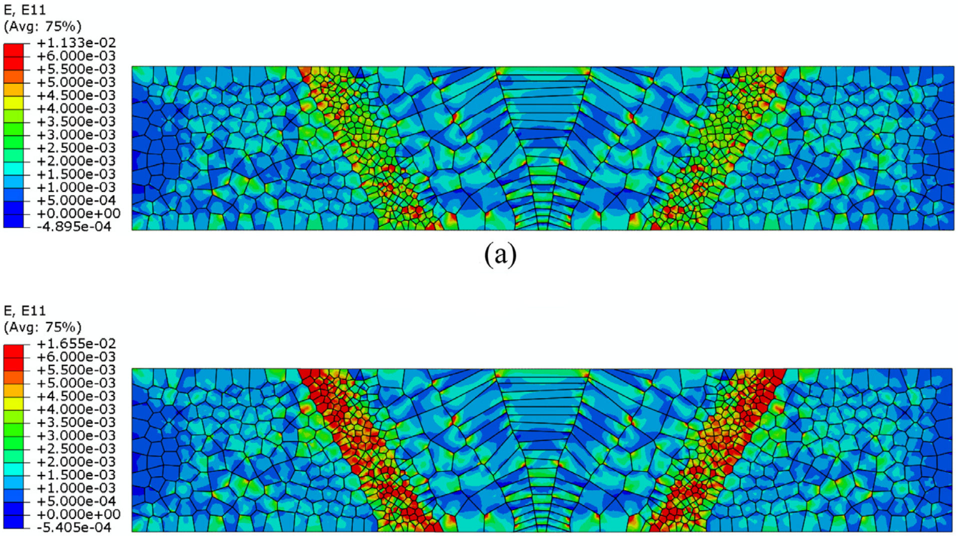

(a)

(b)

Fig. 11. Contour plot of strain distribution after 85 hours creep at 650 °C and 70 MPa (a) for non-standard condition weldment, and (b) for standard condition weldment, involving the contribution of the grain size dependent Coble creep, material strength dependent dislocation creep as well as grain boundary sliding.

take the dominant role for the creep deformation due to the prominent dislocation movements while increasing the applied stresses and temperatures.

6.3. Grain boundary sliding

In addition to the grain interior creep deformation (Section 6.2), grain boundary sliding is also incorporated to investigate the high temperature deformation response of Grade 91 steel weldments. In the present study, GB sliding is assumed to follow the Newtonian viscous flow, and the viscosity parameters are assumed to be same for all the grain boundaries in both non-standard and standard pre-welding tempered welds. Fig. 11 shows the simulation results of strain field for both the non-standard and standard weldments after 85 h creep. The average strain in the fine grained HAZ of the standard and non-standard conditions is about 1.52% and 0.45%, respectively, which shows quantitative agreement with the experimental measurement (Fig. 3(a)). The localized strain of FGHAZ contains the plastic deformation induced by Coble creep, dislocation creep, as well as GB sliding. It is clear GB sliding brings more creep strain accumulation in the fine grained HAZ compared with the strain field of Section 6.2.

There are several reasons for the highly concentrated strain while adding GB sliding. First, the creep strain caused by sliding of grains against one another is more significant in the fine grained HAZ due to the high boundary to volume ratio. This is consistent with the general effect of GB sliding as it can control the strain rate of small-grained materials at high temperatures and intermediate stresses. Moreover, it is interesting that FGHAZs of both standard and nonstandard conditions have fine grained microstructures. Nevertheless, GB sliding results in more creep deformation in the standard condition (~0.84%) than the non-standard condition. This implies the strong interaction between GB sliding and grain interior creep deformation. As GB sliding leads to stress concentration in the vicinity of triple junctions, the high stress can trigger more dislocation creep in the 'soft' FGHAZ of the standard weldment. Also, the higher triaxial stresses, owing to the mechanical constraint of HAZ from base metal and weld metal, are more likely to assist GB sliding in FGHAZ of the standard weldment. Overall, the high creep strain in the FGHAZ contains the contribution of both GB sliding and the dislocation creep due to the interaction of GB sliding with grain interior. Based on the numerical simulations, it is concluded that GB sliding depends on both the microstructure gradients and the hardness distribution in the weldments. It is observed the deformation becomes non-uniform with the increased contribution of GB sliding. In practical measurements, DIC does not capture these fluctuations on the grain scale because of the resolution.

In the CSEF steel weldments, it is the interplay between the response of grain interior and grain boundaries that dictates the overall deformation. The microstructure-informed constitutive model enables us to numerically study the competition among the thermally activated diffusional flow, dislocation motion and grain boundary sliding. Fig. 12 shows the contribution of each deformation mechanism for the total creep deformation of Grade 91 steel weldments (with the strain extracted from a path along half-height of the weldment). For the non-standard pre-welding tempered weldment, Coble creep and grain boundary sliding provide equally 45% of the creep strain in the FGHAZ, and the dislocation creep provides the reminder 10%. The strain accumulation in the non-standard condition is mainly due to the fine grains in the HAZ. For the

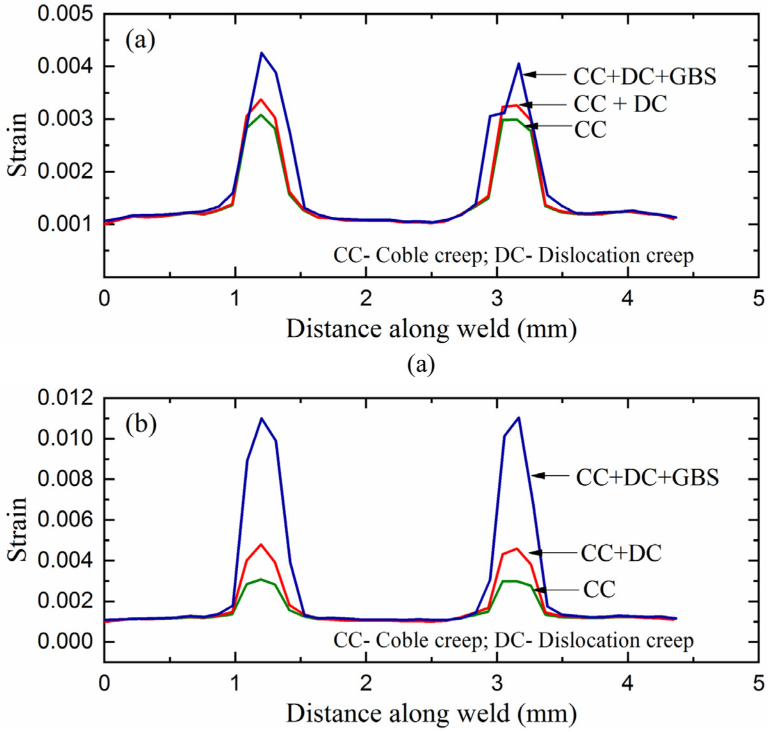

(a)

(b)

Fig. 12. The quantitative contribution of Coble creep, dislocation creep and grain boundary sliding to the total creep strain concentration in the fine grained HAZ, (a) for the non-standard pre-weld tempering weldment and (b) for the standard pre-weld tempering weldment.

standard condition, 'GB sliding' acting as the dominant deformation mechanism provides approximately 65% of the creep strain in the FGHAZ, dislocation creep becomes more important (20%) with the reduced hardness, and Coble creep provides the remaining 15% of the creep strain. It should be noted 'GB sliding' contains the contribution of both GB sliding and the 'extra' dislocation creep. Overall, the strain concentration in the standard condition is caused by both the microstructure gradients and hardness variation in the welded joints. By employing the numerical simulations in Sections 6.1–6.3, the relative significance of each deformation mechanism for the non-standard and standard treatment weldment is quantified step-by-step.

It is noted the numerical results of dislocation creep may have slight deviation from its actual contribution, as GB sliding can influence the triaxial stress and also bring the extra dislocation creep due to the stress concentration in the HAZ. The present work studies the creep deformation of Grade 91 steel weldments at 70MPa and 650°C, in which all deformation mechanisms contribute comparably. The present model can be reliably extended to welded joints under other loading conditions. It can be postulated that contribution of dislocation creep will become more important while increasing the temperature or applied stress because of the accelerated dislocation movements (short-term creep usually performed at laboratory condition); GB sliding will be the rate controlling deformation mechanism at intermediate stress, especially in fine grained materials; and Coble creep will take the lead role at low stresses and temperatures owing to the low activation energy of GB diffusion (long-term creep), which is believed to be the major contributor to the deformation of CSEF steels and the welded joints in application service conditions.

Due to the high constraint of HAZ from the adjacent strong weld metal and base metal, the triaxial stress state is formed and dominant in this region. The stress triaxiality factor is defined as the ratio between the mean stress σ_{m}, and equivalent von-Mises stress σ_{e},

$$TF = \frac{\sigma_{\mathrm{m}}}{\sigma_{\mathrm{e}}} = \frac{1/3(\sigma_1 + \sigma_2 + \sigma_3)}{\frac{1}{2}\sqrt{(\sigma_1 - \sigma_2)^2 + (\sigma_2 - \sigma_3)^2 + (\sigma_3 - \sigma_1)^2}} \tag{10}$$

where σ_1, σ_2 and σ_3 are principle stresses. Fig. 13 shows the distribution of stress triaxiality of the standard pre-welding tempered weldment. Considering the weldment solely deformed by the grain interior creep (Section 6.2), the stress triaxiality is uniformly concentrated near the center of FGHAZ, as shown in Fig. 13(a). While introducing GB sliding (Section 6.3), the distribution of stress triaxiality becomes non-uniform, and there is highly localized triaxial stress in the FGHAZ (Fig. 13(b)). The average stress triaxiality factors for base metal and FGHAZ are calculated as 0.500 and 0.823 for the weldment in absence of GB sliding, respectively, while in presence of GB sliding, the average stress triaxiality factors for base

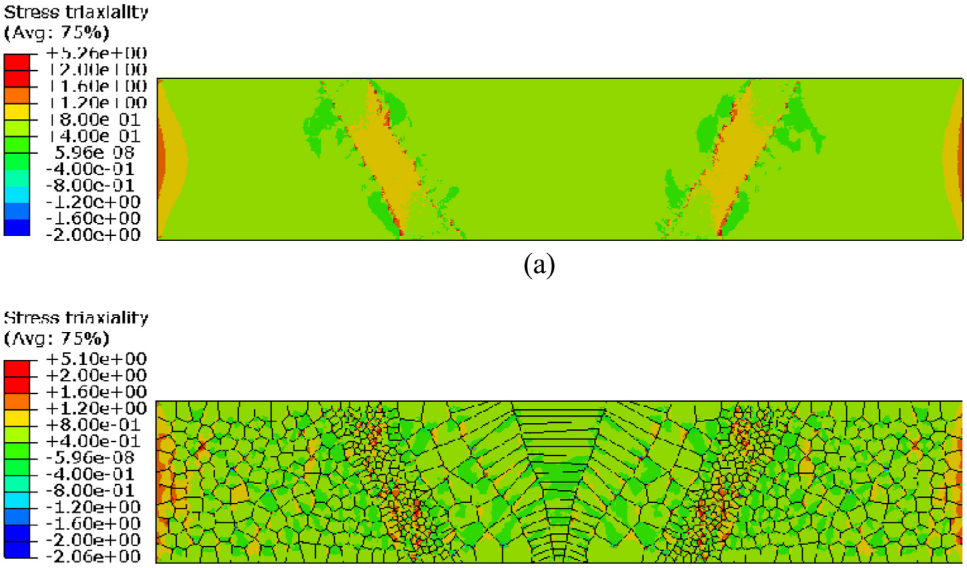

(a)

(b)

Fig. 13. Stress triaxiality for standard pre-weld tempering weldment with the creep deformation accounting for (a) only Coble creep and dislocation creep, and (b) Coble creep, dislocation creep and GB sliding.

metal and FGHAZ sliding are 0.501 and 0.696. Note there is minor concentration of triaxial stress at the triple junctions in the base metal (Fig. 13(b)), but the overall average triaxial stress of the base metal is not influenced by the GB sliding. Although the average of stress triaxiality in the FGHAZ has been reduced and relaxed because of GB sliding, there is strongly localized triaxial stress the vicinity of the triple junctions. According to the vacancy diffusion theory, vacancies diffuse from regions of lower triaxiality to those of higher triaxiality. The high triaxial stresses in FGHAZ are expected to accelerate vacancy accumulation and creep cavitation along grain boundary facets at high temperatures (Abe et al., 2008). The location of Type IV cracking is found to be consistent with the region where the stress triaxiality factor is high (Watanabe et al., 2006; Shinozaki and Kuroki, 2003; Yaguchi et al., 2010; Zhao et al., 2012). Therefore, evaluating the stress multiaxiality is important for predicting the Type IV failure of CSEF steel weldments.

The present work shows the HAZ region has a combination of strain concentration and high stress triaxiality, which possibly leads to early cavity nucleation, its growth and further coalescence towards to the critical failure. The computational approach for investigation of deformation and damage mechanisms responsible for the Type IV failure of CSEF steel weldments, as well as the lifetime prediction will be presented in the companion paper (Part II).

7. Conclusions

We have developed a microstructure-informed, mechanisms-based finite-element model to numerically study the high temperature deformation behavior of CSEF steel weldments. A creep constitutive model which accounts for the dislocation creep and Coble creep (diffusional creep) is used for the grain interior plasticity, and a Newtonian viscous model is employed to describe grain boundary sliding. The numerical results of strain field distribution show encouraging quantitative agreement with DIC measurement, particularly illustrating the effect of pre-welding tempering on the evolution of strain localization in HAZ of ferritic steel weldments. The thermally activated dislocation creep, diffusional creep as well as grain boundary sliding all contribute to the high temperature deformation of ferritic steel weldments, and their relative significance to the total strain accumulation in the fine grained HAZ is quantified owing to our explicit microstructure-based model. For the non-standard pre-welding tempering condition, the strain concentration in the FGHAZ is mainly contributed by the grain size dependent Coble creep and grain boundary sliding. For the standard pre-welding tempering condition, the strain concentration is as a result of the strong interaction between the fine grains and low creep strength of the FGHAZ, in which grain boundary sliding acts as the dominant deformation mechanism. The effects of weldment heterogeneities, including the large grain size gradients in the microstructure and the variation of material hardness, on high temperature creep deformation are numerically studied. The computational simulations provide valuable insights of the micromechanical and microstructural origins for the strain localization in fine-grained HAZ of CSEF steel weldments.

Declaration of Competing Interest

The authors declare no competing interests.

Acknowledgment

The authors are grateful to financial support by the U.S. Department of Energy, Cross-Cutting Materials R&D Program. Additionally, XW acknowledges partial support from the Center for Materials Processing at The University of Tennessee, Knoxville, and YFG acknowledges National Science Foundation DMR 1809640.

Supplementary materials

Supplementary material associated with this article can be found, in the online version, at doi:10.1016/j.jmps.2019.103774.

References

ABAQUS, C., 2012. Analysis User's Manual, Version 6.12, ABAQUS.
Abe, F., 2016. Progress in creep-resistant steels for high efficiency coal-fired power plants. J. Press. Vessel. Technol. 138 (4), 040804.
Abe, F, Kern, T.-U, Viswanathan, R, 2008. Creep-Resistant Steels. Elsevier.
Abe, F., Tabuchi, M., 2004. Microstructure and creep strength of welds in advanced ferritic power plant steels. Sci. Technol. Weld. Join. 9 (1), 22–30.
Abson, D., Rothwell, J., 2013. Review of type IV cracking of weldments in 9–12% Cr creep strength enhanced ferritic steels. Int. Mater. Rev. 58 (8), 437–473.
Albert, S., Matsui, M., Hongo, H., Watanabe, T., Kubo, K., Tabuchi, M., 2004. Creep rupture properties of HAZs of a high Cr ferritic steel simulated by a weld simulator. Int. J. Press. Vessel. Pip. 81 (3), 221–234.
ASTM specification A387, 2008. ASTM International, West Conshohocken PA.
Basirat, M., Shrestha, T., Barannyk, L.L., Potirniche, G.P., Charit, I., 2015. A Creep Damage Model for High-Temperature Deformation and Failure of 9Cr-1Mo Steel Weldments. Metals 5 (3), 1487–1506.
Basirat, M., Shrestha, T., Potirniche, G., Charit, I., Rink, K., 2012. A study of the creep behavior of modified 9Cr–1Mo steel using continuum-damage modeling. Int. J. Plast. 37, 95–107.
Bower, A.F., Wininger, E., 2004. A two-dimensional finite element method for simulating the constitutive response and microstructure of polycrystals during high temperature plastic deformation. J. Mech. Phys. Solids 52 (6), 1289–1317.
Choudhary, B., Samuel, E.I., 2011. Creep behaviour of modified 9Cr–1Mo ferritic steel. J. Nucl. Mater. 412 (1), 82–89.
Coble, R., 1963. A model for boundary diffusion controlled creep in polycrystalline materials. J. Appl. Phys. 34 (6), 1679–1682.
Eggeler, G., Ramteke, A., Coleman, M., Chew, B., Peter, G., Burblies, A., Hald, J., Jefferey, C., Rantala, J., Mohrmann, R., 1994. Analysis of creep in a welded 'P91'pressure vessel. Int. J. Press. Vessel. Pip. 60 (3), 237–257.
Espositoa, L., 2016. Type IV creep cracking of welded joints: numerical study of the grain size effect in HAZ. Proc. Struct. Integr. 2, 919–926.
Francis, J., Mazur, W., Bhadeshia, H., 2006. Review type IV cracking in ferritic power plant steels. Mater. Sci. Technol. 22 (12), 1387–1395.
Frost, H.J., Ashby, M.F, 1982. Deformation Mechanism Maps: the Plasticity and Creep of Metals and Ceramics.
Gaffard, V., Gourgues-Lorenzon, A.-F., Besson, J., 2005. High temperature creep flow and damage properties of 9Cr1MoNbV steels: Base metal and weldment. Nucl. Eng. Des. 235 (24), 2547–2562.
Gifkins, R.C., 1976. Grain-boundary sliding and its accommodation during creep and superplasticity. Metall. Trans. A 7 (8), 1225–1232.
Hall, F., Hayhurst, D., 1991. Continuum damage mechanics modelling of high temperature deformation and failure in a pipe weldment. Proc. R. Soc. Lond. A 433 (1888), 383–403.
Hayhurst, R., Mustata, R., Hayhurst, D., 2005. Creep constitutive equations for parent, Type IV, R-HAZ, CG-HAZ and weld material in the range 565–640 C for Cr–Mo–V weldments. Int. J. Press. Vessel. Pip. 82 (2), 137–144.
Herring, C., 1950. Diffusional viscosity of a polycrystalline solid. J. Appl. Phys. 21 (5), 437–445.
Huang, Y., 1991. A User-Material Subroutine Incroporating Single Crystal Plasticity in the ABAQUS Finite Element Program. Harvard University.
Kimmins, S., Smith, D., 1998. On the relaxation of interface stresses during creep of ferritic steel weldments. J. Strain Anal. Eng. Des. 33 (3), 195–206.
Kimura, K., Sawada, K., Kushima, H., Toda, Y., 2007. Long-term creep strength of creep strength enhanced ferritic steels. Chall. Power Eng. Environ. 1059–1065.
Li, D.-F., Barrett, R.A., O'Donoghue, P.E., Hyde, C.J., O'Dowd, N.P., Leen, S.B., 2016. Micromechanical finite element modelling of thermo-mechanical fatigue for P91 steels. Int. J. Fatigue 87, 192–202.
Li, D.-F., Barrett, R.A., O'Donoghue, P.E., O'Dowd, N.P., Leen, S.B., 2017. A multi-scale crystal plasticity model for cyclic plasticity and low-cycle fatigue in a precipitate-strengthened steel at elevated temperature. J. Mech. Phys. Solids 101, 44–62.
Li, D.-F., Golden, B.J., O'Dowd, N.P., 2014. Multiscale modelling of mechanical response in a martensitic steel: a micromechanical and length-scale-dependent framework for precipitate hardening. Acta Mater. 80, 445–456.
Li, S., Zhou, J., Ma, L., Xu, N., Zhu, R., He, X., 2009. Continuum level simulation on the deformation behavior of nanocrystalline nickel. Comput. Mater. Sci. 45 (2), 390–397.
Masse, T., Lejeail, Y., 2013. Creep mechanical behaviour of modified 9Cr1Mo steel weldments: experimental analysis and modelling. Nucl. Eng. Des. 254, 97–110.
Meade, E.D., Sun, F., Tiernan, P., O'Dowd, N.P., 2018. Experimental study and multiscale modelling of the high temperature deformation of tempered martensite under multiaxial loading. Mater. Sci. Eng. A 737, 383–392.
Mukherjee, A.K., Bird, J.E., Dorn, J.E., 1969. Experimental correlations for high-temperature creep. Trans. Am. Sot. Metals 62, 155.
Nabarro, F., 1967. Steady-state diffusional creep. Philos. Mag. 16 (140), 231–237.
Nieh, T., Hsiung, L., Wadsworth, J., Kaibyshev, R. High strain rate superplasticity in a continuously recrystallized Al–6% Mg–0.3% Sc alloy, Acta Mater. 46(8) (1998) 2789-2800.
Nieh, T.-G., Wadsworth, J., Sherby, O.D., 2005. Superplasticity in Metals and Ceramics. Cambridge University Press.
NIMS creep data sheet No. 43, 1996.
Otoguro, Y., Matsubara, M., Itoh, I., Nakazawa, T., 2000. Creep rupture strength of heat affected zone for 9Cr ferritic heat resisting steels. Nucl. Eng. Des. 196 (1), 51–61.
Petry, C., Gariboldi, E., 2010. Experimental characterisation and modelling of the creep properties of a P92 steel weldment. Mater. High Temp. 27 (1), 1–10.
Quey, R., Dawson, P., Barbe, F., 2011. Large-scale 3D random polycrystals for the finite element method: generation, meshing and remeshing. Comput. Methods Appl. Mech. Eng. 200 (17-20), 1729–1745.
Raabe, D., Sachtleber, M., Zhao, Z., Roters, F., Zaefferer, S., 2001. Micromechanical and macromechanical effects in grain scale polycrystal plasticity experimentation and simulation. Acta Mater. 49 (17), 3433–3441.
Shinozaki, K., Kuroki, H., 2003. Stress-strain analysis of creep deterioration in heat affected weld zone in high Cr ferritic heat resistant steel. Mater. Sci. Technol. 19 (9), 1253–1260.
Shrestha, T., Basirat, M., Charit, I., Potirniche, G.P., Rink, K.K., Sahaym, U., 2012. Creep deformation mechanisms in modified 9Cr–1Mo steel. J. Nucl. Mater. 423 (1-3), 110–119.
Solutions, C., 2010. Vic-3D Manual. Correlated Solutions, Inc, Columbia, SC.
Sun, F., Meade, E.D., Noel, P., 2018. Microscale modelling of the deformation of a martensitic steel using the Voronoi tessellation method. J. Mech. Phys. Solids 113, 35–55.

Sun, F., Meade, E.D., O'Dowd, N.P., 2019. Strain gradient crystal plasticity modelling of size effects in a hierarchical martensitic steel using the Voronoi tessellation method. Int. J. Plast. 119, 215–229.

Tabuchi, M., Hongo, H., Li, Y., Watanabe, T., Takahashi, Y., 2009. Evaluation of microstructures and creep damages in the HAZ of P91 steel weldment. J. Pressure Vessel. Technol. 131 (2), 021406.

Tabuchi, M., Watanabe, T., Kubo, K., Matsui, M., Kinugawa, J., Abe, F., 2001. Creep crack growth behavior in the HAZ of weldments of W containing high Cr steel. Int. J. Press. Vessel. Pip. 78 (11-12), 779–784.

Watanabe, T., Tabuchi, M., Yamazaki, M., Hongo, H., Tanabe, T., 2006. Creep damage evaluation of 9Cr–1Mo–V–Nb steel welded joints showing Type IV fracture. Int. J. Press. Vessel. Pip. 83 (1), 63–71.

Wei, Y., Bower, A.F., Gao, H, 2007. Recoverable creep deformation due to heterogeneous grain-boundary diffusion and sliding. Scr. Mater. 57 (10), 933–936.

Wei, Y., Bower, A.F., Gao, H., 2008. Recoverable creep deformation and transient local stress concentration due to heterogeneous grain-boundary diffusion and sliding in polycrystalline solids. J. Mech. Phys. Solids 56 (4), 1460–1483.

Yaguchi, M., Ogata, T., Sakai, T., 2010. Creep strength of high chromium steels welded parts under multiaxial stress conditions. Int. J. Press. Vessel. Pip. 87 (6), 357–364.

Yu, X., Babu, S.S., Terasaki, H., Komizo, Y., Yamamoto, Y., Santella, M.L., 2013. Correlation of precipitate stability to increased creep resistance of Cr–Mo steel welds. Acta Mater. 61 (6), 2194–2206.

Yu, X., Feng, Z., Yamamoto, Y., 2014. In-Situ Full Field Creep Deformation Study of Creep Resistant Materials Welds. Oak Ridge National Lab.(ORNL), Oak Ridge, TNUnited States.

Zhao, L., Jing, H., Xu, L., Han, Y., Xiu, J., 2012. Analysis of creep crack growth behavior of P92 steel welded joint by experiment and numerical simulation. Mater. Sci. Eng. A 558, 119–128.